World Scientific
www.worldscientific.com

DeepJoint Segmentation-based Lung Segmentation and Hybrid Optimization-Enabled Deep Learning for Lung Nodule Classification

P. Chinniah*

Professor, Department of Electronics & Communication Engineering
St.Joseph College of Engineering
Sriperumbudur, Chennai, Tamil Nadu, India
chinnaiah.p@gmail.com

Balajee Maram

Chitkara University School of Engineering and Technology
Chitkara University, Baddi, Himachal Pradesh, India

P. Velrajkumar

Associate Professor, Department of Electrical & Electronics Engineering
CMR Institute of Technology
Bengaluru, India

Ch. Vidyadhari

Assistant Professor, Department of Information Technology
Gokaraju Rangaraju Institute of Engineering and Technology
Bachupally, Hyderabad, India

Lung cancer is an aggressive disease among all cancer-based diseases, because of causing huge mortality in humans. Thus, earlier discovery is a basic task for diagnosing lung cancer and it helps increase the survival rate. Computed tomography (CT) is a powerful imaging technique used to discover lung cancer. However, it is time-consuming for examining each CT image. This paper develops an optimized deep model for classifying the lung nodules. Here, the pre-processing is done using Region of Interest (ROI) extraction and adaptive Wiener filter. The segmentation is done using the DeepJoint model wherein distance is computed with a congruence coefficient for extracting the segments. The nodule identification is done by a grid-based scheme. The features such as Global Binary Pattern (GBP), Texton features, statistical features, perimeter and area, barycenter difference, number of slices, short axis and long axis and volume are considered. The lung nodule classification is done to classify part solid, solid nodules

---

*Corresponding author.

and ground-glass opacity (GGO) using Deep Residual Network (DRN), which is trained by the proposed Shuffled Shepard Sine–Cosine Algorithm (SSSCA). The developed SSSCA is generated by the integration of the Sine–Cosine Algorithm (SCA) and Shuffled Shepard Optimization Algorithm (SSOA). The proposed SSSCA-based DRN outperformed with the highest testing accuracy of 92.5%, sensitivity of 93.2%, specificity of 83.7% and F_1-score of 81.5%.

Keywords: Computed tomography images; DeepJoint model; Deep Residual Network; grid-based scheme; lung nodule classification.

1. Introduction

Lung cancer is an aggressive disease among all cancer-based diseases, because of causing huge mortality in humans, and the standard five-year rate of survival in the patient is lesser than 20%, even though there exist beleaguered diagnoses and several chemotherapies and radiotherapy regimens. The average time of survival for a patient with advanced lung cancer is 12 months.[16] Thus, earlier discovery, earlier treatment and earlier diagnosis of lung cancer can efficiently enhance the quality of life and rate of survival of the patients. A smudge on the lung computed tomography (CT) image is described as a lung nodule (LN) that can be either malignant or benign. Earlier lesions of the lung are mostly characterized by spiteful nodules in the lungs. Thus, it is essential for scientific treatment of lung cancer for classifying the nodules of the lung in a precise manner. Recently, the enhancement of health levels and development of medical facilities have gained popularity among the researchers.[10,27,28] Several subtle lesions can be accumulated by an imaging tool. Among them, CT is known to be the most effective tool, which can discover lung cancer earlier. Doctors are required to treat malignant nodules by precisely reading the CT image, but reading a huge number of CT images takes more time, and thus there exists a large probability for misdiagnosis. Due to the design of information technology, computer-based detection modules using CT have provided effective outcomes.[2,29] Among several diseases, lung cancer is an abandoned design of cells in an unequivocal region.[11]

Cancer in the lung is identified through the existence of nodules, which reveal the stage of the problem being examined.[12] It can be differentiated at the starting phase, due to the existence of only fewer pulmonary nodules, and distinct methods are used for identifying whether it is a cancerous nodule or the starting phase. The nodules contained in the lungs help to detect lung tissue alterations considering the norm, which is commonly circular fit with the dimension of mm. The human body contains various cells. Whenever cells expand to the exterior lung, then the nodule of the lung is generated. Some prejudiced settings within 3 mm are termed as miniaturized and those exceeding 3 mm are termed as mass. They are considered cancerous and must be detected at the right time. Generally, the nodules are defined in two formats including benign or mass. If the dimension of the nodule is 3 cm or lesser, then it is known as pulmonary. The shape of lung nodules is usually round and they are perplexing when included within an anatomical model. Identification of the position

of LN can be a complex task, and it is complex to separate as well. There exist various techniques for portraying LNs by densitometry, their development, size and morphology. In recent days, various methods are devised for segmenting the lung and detecting the nodules, and techniques have been developed for nodule segmentation and recognition.[7]

Deep Neural Network (DNN) has been extensively utilized in the processing of images with better outcomes; this field was worth 300 million USD by 2021, but there are two main issues of deep learning including scalability and usability.[13] The input to DNN has manually mined features using different hidden layers. Deep learning considering chest radiology is an active research domain recently.[32,33] Various models are utilized including Recursive Neural Network (RvNN),[14] Convolutional Neural Network (CNN),[25,31] Recurrent Neural Network (RNN), Variational Autoencoder (VAE), Deep Boltzmann Machine (DBM), Generative Adversarial Network (GAN),[17] Deep Belief Network (DBN),[15] Autoencoder, Stacked Autoencoder and Deep Residual Network (DRN).[16,26] Some of the deep learning methods are illustrated as follows. RNN associates the nodes, using a directed graph, and memorizes prior inputs for predicting the output. RvNN is an extraordinary case of RNN that applies a similar group of weights for structured input.[30] Both RNN and RvNN are utilized for natural language processing. DBN represents a deep network with several associated hidden layers and the units of layers are also associated. Deep Boltzmann Machine is comparable to DBN but poses undirected links among the hidden layers.

1.1. *Motivation*

Cancer in the lung is identified through the existence of nodules, revealing the stage of the problem being examined. The major cause is the formation of cancerous nodules around the lungs. Thus, an earlier discovery of nodules is essential. Various methods are devised for lung nodules segmentation and recognition. The problems encountered in the conventional approaches are given as follows:

- In several cases, it is complex to arrive at an accurate treatment because of the complex morphological model of nodules.[4]
- It is difficult to identify the morphological difference between the earlier-phase cancerous nodule and benign nodule.
- Some important features are not considered for the nodule segmentation, which affects the accuracy of the model.

The aforementioned issues and challenges are taken as motivation for designing a new method to classify lung cancer using CT images.

The main aim is to design an approach for lung nodule detection using an optimization-based deep learning technique. First, the inputted CT image is fed to

pre-processing in which the Region of Interest (ROI) extraction and adaptive Wiener filter are applied to discard noise. The segmentation of the lung lobe is done with DeepJoint to accurately segment regions of the lung lobe where the distance is computed based on the congruence coefficient. After the lung lobe segmentation, the nodule identification is carried out using a grid-based scheme. The next phase is the extraction of features like Global Binary Pattern (GBP), Texton features, perimeter and area, barycenter difference, number of slices, volume, short axis and long axis and statistical features being considered for the enhanced process. After feature mining, the extracted features are subjected to lung nodule classification where the nodule region is classified into ground-glass opacity (GGO), part solid and solid nodules with DRN, which is trained with the proposed Shuffled Shepard Sine–Cosine Algorithm (SSSCA). The SSSCA is developed by integrating Shuffled Shepard Optimization Algorithm (SSOA) and Sine–Cosine Algorithm (SCA).

The major contributions of the paper are as follows:

- Proposed SSSCA-based DRN for lung nodule classification: The proposed SSSCA-based DRN is utilized for classifying the lung nodules into GGO, part solid and solid nodules. The DRN training is done with the devised SSSCA, which is developed by combining SSOA and SCA.

The remaining sections are organized as follows: Section 2 defines the conventional lung nodule classification models. Section 3 presents the proposed model for lung nodule classification. Section 4 defines the efficiency of the proposed technique. Section 5 offers the conclusion.

2. Literature Survey

The eight conventional lung nodule classification methods are described with their advantages and disadvantages. Kuo *et al.*[1] developed a technique for classifying the lung nodules into solid nodules, part solid and GGO using CT images. Here, the edge searching method was utilized for segmenting the lungs. To mine the nodules with distributed gray levels, the accumulation of images was utilized for enhancing the nodules to improve the gray level of each of them. Support Vector Machine (SVM) was utilized for classifying the lung nodules. However, the SVM required more time for optimizing the kernel function. Wu *et al.*[2] utilized a DRN for classifying the lung nodules using the CT images. Here, the ResNet network structure was utilized to enhance the image. Then, the DRN was utilized by integrating migration learning and residual learning. The degradation of network efficiency is a major issue, due to the huge network depth. Wang *et al.*[3] utilized CNN with CT images for the lung nodules classification. Here, the raw CT image patches were integrated with CNN for reducing the system complexity. Also, the CT image was split into various patches that were divided into six kinds. However, the method failed to classify malevolent nodule types. El Hassani *et al.*[4] developed Discrete Cosine Transform (DCT) with

CNN for effective categorization of lung nodules. Here, the DCT and CNN were integrated for providing enhanced accuracy. However, the nonnodule regions were complex to detect which affected the performance of classification. de Nobrega *et al.*[5] utilized deep transfer learning to classify cancer. Here, 1 018 chest CT examinations were utilized for medical annotations. Also, seven CNNs were constructed using the ImageNet dataset. Then, each group of deep features was utilized for classification. However, this technique did not automatically segment lung nodules. Huang *et al.*[6] developed Deep Transfer Convolutional Neural Network (DTCNN) and Extreme Learning Machine (ELM) for classifying lung cancer. Here, the optimum DTCNN was employed for mining the features to train ImageNet. Then, ELM was utilized to categorize benign and malignant lung nodules. However, the memory consumption of this method was very high. Veronica[7] designed a technique for classifying lung nodules using CT. Here, the precise portion of the lung image was achieved and fed to pre-processing in which the level of image contrast was improved by adjusting the function. Also, the nodules were segmented with Fuzzy *C*-Means (FCM) for effectual nodule classification. If the sizes of the nodules were too small, then it may result in wrong classification outcomes. Zhang and Kong[8] developed a Multi-scene Deep Learning Framework (MSDLF) for the effectual classification of lung nodules. Here, a CNN was utilized for improving the knowledge of radiologists in determining the four-phase nodules. The method was effective and increased the accuracy, but the speed of processing was very high.

2.1. *Challenges*

The problems confronted by the conventional lung nodule classification methods are enlisted as follows:

- In Ref. 6, the DTCNN–ELM method was developed for classifying the lung nodules using CT images. However, the major issue is the examination of various transfer learning methods and ELM structures for making them robust.
- In Ref. 7, the major goal of the technique was to enhance the accuracy of classification by mining some specific features of lung images.
- In several cases, it is complex to arrive at a precise treatment because of the complex morphological model of nodules.[4]
- In Ref. 3, the CNN was utilized for detecting the nodules of lungs, but the deficiency of huge training sets of lung nodules and low sensitivity were the issues. Hence, the important issue is the reliance of CNN on huge training sets.
- The major issue in determining lung cancer is categorizing benign nodules and cancerous lesions, which are detected by noninvasive and invasive techniques. Thus, there is a requirement for a sophisticated deep learning method for identifying the morphological difference between earlier-phase cancerous nodules and benign nodules.

3. Proposed SSSCA-based DRN for Lung Nodule Classification

Cancer is a major disease about which people are specifically concerned nowadays. The major cause is the formation of cancerous nodules around the lungs. Thus the earlier discovery of nodules is essential. The aim is to present an approach for detecting lung nodules considering the optimization-based DRN. First, the input CT is subjected to the ROI extraction phase with an adaptive Wiener filter. The segmentation of the lung lobe is performed using the DeepJoint model[19] for precisely segmenting the regions of the lung lobe in which the distance is computed using the congruence coefficient. With a segmented lung lobe, the nodule identification is done with a grid-based scheme. Certain features like GBP, Texton features, statistical features, perimeter and area, barycenter difference, number of slices, short axis and long axis and volume are adapted for improved processing. After the feature extraction phase, the obtained features are subjected to lung nodule classification where the nodule region is classified into GGO, part solid and solid nodules with DRN,[20] which is trained using SSSCA. The SSSCA is devised by combining SSOA[21] and SCA.[22] The architecture of lung nodule detection using the proposed SSSCA-based DRN is displayed in Fig. 1.
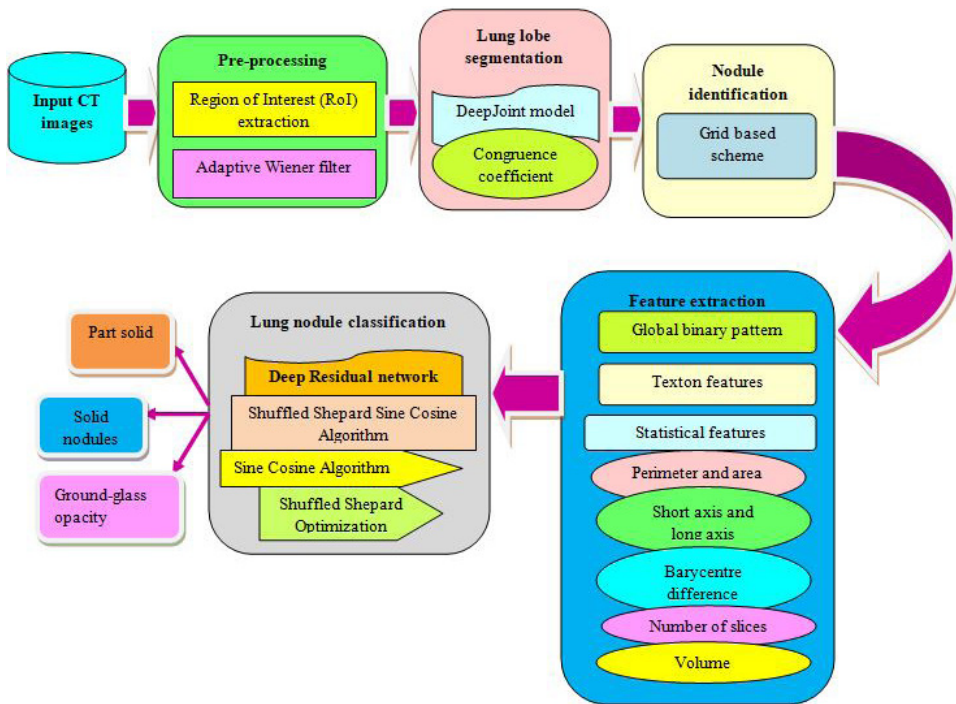

Fig. 1.   Architecture of lung nodule classification using the developed SSSCA-based DRN.

Table 1.   Symbols table.

r	Total number of images
Q	Database
I_s	The sth input image
J	Windows length
K	Windows width
L	Inputted image value chosen in the window size
l_1, l_2	Original image coordinates selected from the window size
B	Original image
m_2	Noise variance
I_s	Pre-processed image
m_f	The fth grid
g	Total grids
G_n	Values of pixel linked to grid M_j
I	Count of pixels in grid M_j
α	Threshold
F_g	Value of mean
G_w^x	Joined pixels in specific grid m_g
D	Total joined pixels in f_g
t	Number of mapped points
ϑ_l	Missed pixel
κ	Total missed pixels
C	Output produced from DeepJoint model
E	Region of nodule segment
a_2	Gradient in horizontal direction
a_4	Gradient in vertical direction
a_1, a_3	Gradients with diagonal directions
(u, w)	Pixel location
V_1, V_2, V_3, V_4	Values of pixels
$P = (c, d)$	Position of pixel
W_1, W_2, W_3, W_4, W_5	Five pixel values
$O \times N$	Total pixel positions
$s(u, w)$	Position of sth pixel
k	Block area or count of pixels
ν	Count of pixels length
ω	Short axis of object
ϑ	Long axis of object
ϖ	Coordinate of barycenter point of object
s	Area of object
$n(i, j)$	Gray-scale value of image at the coordinate (i, j)
z	Difference of barycenters
ϖ_1	Barycenter of pre-image
ϖ_2	Barycenter of current image
ϖ_3	Barycenter of post-image
R_1	GBP features
R_2	Texton features
R_3	Mean
R_4	Variance
R_5	Standard deviation
R_6	Kurtosis
R_7	Skewness
R_8	Perimeter and area
R_9	Short axis and long axis

Table 1.   (*Continued*)

R_{10}	Barycenter difference
R_{11}	Number of slices
R_{12}	Volume
M	CNN feature
(x, y)	Record coordinates
G	$E * E$ kernel matrix
a, s	Position indexes
G_z	Kernel size for zth input neuron
$*$	Cross-correlation operator
a_{in}	Input matrix width
s_{in}	Input matrix height
a_{out}, s_{out}	Values of output
Z_a	Kernel size width
Z_s	Height of kernel size
K	Feature
M	Residual block input
N	Residual block output
$\Re$	Residual function
λ_m	Dimension matching factor
λ	Weight matrix
τ	Bias
Y	Output of DRN
U_x^0	Initial solution vector of xth sheep
U_{max}, U_{min}	Bounds of design variables
rand	Random vector in [0,1]
j	Number of sheep
ξ_f	Output to be expected
U_x, U_o, U_a	Solution vectors of shepherd chosen, horse and chosen sheep in m-directional search space
μ, η	Parameters
U_x^{temple}	Temple solution vector
U_x^{old}	Old solution vector
λ_x	Step size
$U(z)$	Current solution
d_1, d_2, d_3	Random numbers
QB	Current position of destination point
$\|$	Absolute value
c	True positive
e	True negative
f	False positive
d	False negative

Initially, the inputted images are accumulated for lung nodule classification. Consider a dataset Q with R images that is represented as

$$Q = I_1, I_2, \ldots, I_s, \ldots, I_r. \tag{1}$$

Hence, the image I_s is subjected to pre-processing to eliminate noise contained in it.

3.1. *Pre-processing to discard noise*

Pre-processing helps in converting unstructured data into structured one. Furthermore, it helps to smooth the distortions and enhance features of the image that assist in improved processing. Thus, the image is subjected to pre-processing which is termed an imperative step in computing data. The implication of pre-processing is to provide enhanced processing.

(i) ROI extraction. ROI is discovered with pixel intensity values using resultant masking. The process of scrambling concerned regions with uninteresting ones is performed in this step. Whenever the user defines a gray-scale intensity value using the dependent regions and beneath section expresses background, then the image is expected to fall within the threshold known as thresholding. The intensity values of ROI are considered as density slices in which the adjacent discovery of pixels has a value of either 1 or 0.

(ii) Adaptive Wiener filter. The adaptive Wiener filter[1] utilizes an image noise filtering technique for discarding the noises that came from manual operation, vibration of the machine and image reconstruction defects from the input image. This optimizes the image and helps to judge the position of the object and contour in a precise manner. The Wiener filter can effectually keep the edge of the image and minimize the noise from the filter in which the estimation is done using variance and regional average for replacing the gray level. Here, the regional average is given as

$$e = \frac{1}{JK} \sum_{l_1,l_2 \in L} B(L_1, L_2). \tag{2}$$

The variance is given as

$$\sigma^2 = \frac{1}{JK} \sum_{l_1,l_2 \in L} B^2(l_1, l_2) - e^2. \tag{3}$$

The coordinates are given as

$$F(l_1, l_2) = e + \frac{\sigma^2 - m^2}{\sigma^2} (B(l_1, l_2) - e). \tag{4}$$

Thus, the pre-processed image I_s is fed as an input to the segmentation module.

3.2. *Segmentation of lung lobe using DeepJoint model*

The pre-processed image I_s is fed as an input for segmentation of the lung lobe performed with the DeepJoint model[19] by evaluating the optimum values of threshold. Here, I_s is given to DeepJoint that identifies the best segments. The steps undergone are described in the following:

Step 1 (Grids configuration). First, the image is divided into various grids wherein the grid size is employed as 2×2. The split grids are produced with

pre-processed image, and denoted by

$$M = M_1, M_2, \ldots, M_f, \ldots, M_g. \tag{5}$$

Step 2 (Joining phase). After grid generation, the pixels through intra-grid points are integrated using the threshold and mean. The average values are computed as

$$M_j = \frac{\sum_{n=1}^{I} G_n}{I}. \tag{6}$$

The joining pixels are formulated as

$$M_j = \frac{\sum_{n=1}^{I} G_n}{I} \pm \alpha. \tag{7}$$

Step 3 (Region fusion phase). The region fusion matrix is generated by adapting the allocated grids. The region fusion is carried out using two conditions that must be fulfilled and are expressed as follows:

(i) F_g should be lesser than 3.
(ii) Then selection of a single grid point for each grid is performed.

From the aforementioned conditions, the similarity of the region is discovered and these regions are integrated for discovering the mapped points. The region similarity is given by

$$F_g = \frac{\sum_{w=1}^{D} G_w^X}{G}. \tag{8}$$

The grid which is integrated is known as mapped points, and is given by

$$F = F_1, F_2, \ldots, F_u, \ldots, F_t. \tag{9}$$

Step 4 (Determination of deep points). The deep points are determined by adapting the missed pixels. The residual pixels are termed as missed pixels, and are given by

$$E = \vartheta_l, \quad 1 < l \leq k. \tag{10}$$

Thus, the deep points are computed as

$$K_{\text{points}} = \varepsilon + l_p. \tag{11}$$

Step 5 (Acquisition of best segment). Finally, the best segment is discovered using the deep points by using an iterative technique. Hence, the minimal distance based on the congruence coefficient is given by

$$P^{\text{dist}} = \frac{\sum_{q=1}^{20} A_b \text{E point q}}{\sqrt{\sum_{q=1}^{20} (A_b)^2 \sum_{q=1}^{20} (\text{E point q})^2}}. \tag{12}$$

The output produced from the DeepJoint model is the lung lobe segments, which are denoted as C and from each segment, the nodules are identified.

3.3. *Nodule identification using grid-based scheme*

Once C is obtained, the lung nodule identification is done by adapting the grid-based scheme. Here, it can be effectually determined whether the region of the nodule is affected or not. A grid-based scheme is applied on C to divide the region of segments into a number of blocks known as grids. For making the computation simple and to reduce the time of computation, it is required to divide the segmented image into different blocks. Using the grid-based method, the segmented region is split into various grids for determining the lung nodules. Thus, the region of the nodule is discovered from the segmented image and is denoted by E.

3.4. *Extraction of significant features*

From E, the features are extracted from each segment. Here, the essential features generated with segments and insinuation of mining are examined. The mining of features is performed to generate relevant features for achieving enhanced lung nodule classification. The features extracted with segments are described below. Each feature mined using the segments is briefed here.

(a) *Global Binary Pattern*

It refers to texture operators particularly utilized in computer vision problems, like classification of texture and background subtraction.[23] It reveals each pixel considering the relative dim estimation of the neighboring pixel. The GBP reveals each pixel with its relative gradient at several pixel locations. Assume the 1D masks as $[-101]$ and $[-101]_T$ which are termed as a_2 and a_4. The gradients with diagonal directions are evaluated by adapting two 2D masks as $[001; 000; -100]$ and $[-100; 000; 001]$ which are named as a_1 and a_3. Thus, the value of GBP using u, w is expressed by

$$F_3 = \mu(\|a_1(u,w)\| - \|a_4(u,w)\|) + \mu(\|a_3(u,w)\| - a_4\|(u,w)\|)2$$

$$+ \mu(\|a_1(u,w)\| - \|a_2(u,w)\|)2^2 + \sum_{\hbar=1}^{4} \mu(a\hbar(u,w))2^{7-\hbar}, \tag{13}$$

$$\mu(\wp) = \begin{cases} 1, & \wp \geq 0, \\ 0 & \text{otherwise.} \end{cases} \tag{14}$$

Thus, GBP refers to the value of an integer which lies between 0 and $2^7 - 1$. So, the GBP feature poses a size of $[1 \times 50]$, and is denoted as R_1.

(b) *Texton features*

The Texton features[24] adapted for feature extraction are given below. Consider there are 2×2 grids and the pixel values are expressed as V_1, V_2, V_3 and V_4. If the four values of the pixels are the same, then these pixels are termed as Texton.

Assume $P = (c, d)$ at a similar position. Each Texton image unit contains a value of the pixel and these units of Texton image contain five pixel values that are given by W_1, W_2, W_3, W_4 and W_5. If the five values of the pixels are the same, then the final Texton image is placed with the original value in an equal position. Here, the Texton feature is denoted as R_2.

(c) *Statistical features*

The statistical features are used to accumulate, review and analyze the data to make an effectual decision. The statistical features adapted for the assessment include mean, variance, standard deviation, kurtosis and skewness.

(i) Mean

It is evaluated by summing the values of pixels from the image divided by the total pixels. The mean of the sth pixel (u, w) is evaluated as

$$R_3 = \frac{1}{O \times N} \sum_{u=1}^{O} \sum_{w=1}^{N} s(u, w). \tag{15}$$

(ii) Variance

It refers to the spread of intensity values based on the value of the mean, and is expressed as

$$R_4 = \frac{1}{O \times N} \sum_{u=1}^{O} \sum_{w=1}^{N} (s(u, w) - R_3)^2. \tag{16}$$

(iii) Standard deviation

It refers to the second central moment which reveals the measure of inhomogeneity,

$$R_5 = \frac{1}{O \times N} \sum_{u=1}^{O} \sum_{w=1}^{N} (s(u, w) - R_4)^2. \tag{17}$$

(iv) Kurtosis

The shape of the arbitrary variable probability distribution is indicated with kurtosis which is given by

$$R_6 = \frac{1}{(R_5)^4} \sum_{u=1}^{O} \sum_{w=1}^{N} (s(u, w) - R_4)^4. \tag{18}$$

(v) Skewness

It refers to the measure of symmetry, and is formulated as

$$R_7 = \frac{1}{(R_6)^3} \sum_{u=1}^{O} \sum_{w=1}^{N} (s(u, w) - R_5)^3. \tag{19}$$

(d) *Perimeter and area*

It refers to the circle's circumference in a region. The long objects are differentiated from huge or circular objects and the formula of perimeter and area[1] is

given by

$$R_8 = \frac{k}{\nu}.$$ (20)

(e) *Short axis and long axis*

The short axis and long axis[1] are utilized for differentiating between long and rounded objects in which the long axis of the feature indicates the longest object diameter and the short axis indicates the longest object diameter perpendicular to the long axis, given as

$$R_9 = \frac{\omega}{\vartheta}.$$ (21)

(f) *Barycenter difference*

The barycenter difference[1] is utilized for computing the change of the value of gray scale in the image. Each object present in the nodule is utilized for computing the barycenters of pre-image, current image and post-image. The barycenter utilizes the values of gray scale and weights, and thus the object barycenter is generated that is given as

$$\varpi = \left[\frac{\sum_{i,j \in S} n(i,j) \times i}{\sum_{i,j \in S} n(i,j)}, \frac{\sum_{i,j \in S} n(i,j) \times j}{\sum_{i,j \in S} n(i,j)} \right].$$ (22)

The system discovers a minimum of effectual nodule contours, and thus the successive barycentric coordinates are utilized for computing the difference that is given as

$$Z = \sqrt{(\varpi_1)^2 - (\varpi_2)^2} + \sqrt{(\varpi_2)^2 - (\varpi_3)^2}.$$ (23)

The barycenter difference feature is expressed as R_{10}.

(g) *Number of slices*

The number of slices[1] is the count of slices contained in the segment. Here, too less or too many slices means that the object is not a nodule and this feature is expressed as R_{11}.

(h) *Volume*

The volume[1] is indicated as R_{12}.

The feature vector formed considering the computed features is formulated as

$$R = \{R_1, R_2, R_3, R_4, R_5, R_6, R_7, R_8, R_9, R_{10}, R_{11}, R_{12}\}.$$ (24)

3.5. *Classification of lung nodules using the developed SSSCA-based DRN*

The basic operation of classifying the lung nodules is performed using the developed SSSCA-based DRN. The feature vector is considered as the input. Here, the training of DRN is performed with the proposed SSSCA. The DRN structure and training of SSSCA are discussed below.

3.5.1. *Architecture of DRN*

The feature vector is offered as the DRN input. DRN[20] is employed to make an effectual decision concerning the identification of the class of lung nodule. The DRN assists in improving the vanishing-gradient problems and also in reinforcing the features propagation. It assists in reprocessing the features and reducing the count of attributes. It is connected and generates accurate results.

Conv layer: It is used for minimizing free attributes in training and offers reimbursement for sharing the weights. The conv layer assists in processing the input image considering the sequence of the filter. The computation procedure of conv layer is expressed as

$$B2d(M) = \sum_{a=0}^{E-1} \sum_{s=0}^{E-1} X_{a,s} \bullet M_{(x+a),(y+s)}, \tag{25}$$

$$B1d(M) = \sum_{z=0}^{C_{\text{in}}-1} G_Z * M. \tag{26}$$

Pooling layer: It is linked to the conv layer, and utilized for reducing the spatial size of the feature map. Thus, average pooling is selected for functioning on each slice and feature map depth,

$$a_{\text{out}} = \frac{a_{\text{in}} - Z_a}{\lambda} + 1, \tag{27}$$

$$s_{\text{out}} = \frac{s_{\text{in}} - Z_s}{\lambda} + 1. \tag{28}$$

Activation function: It is used to learn the nonlinear and complicated features for enhancing the nonlinearity of mined features. The Rectified Linear Unit (ReLU) is utilized to process the image. The ReLU is given by

$$\text{ReLU}(M) = \begin{cases} 0, & K < 0, \\ K, & K \geq 0. \end{cases} \tag{29}$$

Batch normalization: The group to be trained is split into small groups known as mini-batches to train the model. It attains balance between convergence and evaluation complexity.

Residual blocks: It expresses the shortcut association among conv layers. The dimension matching factor is adapted to match the input and output, which is given by

$$N = \Re(M) + M, \tag{30}$$

$$N = \Re(M) + \Lambda_M M. \tag{31}$$

Linear classifier: After terminating the conv layer, the linear classifier employs a procedure for determining noisy pixels with the input image,
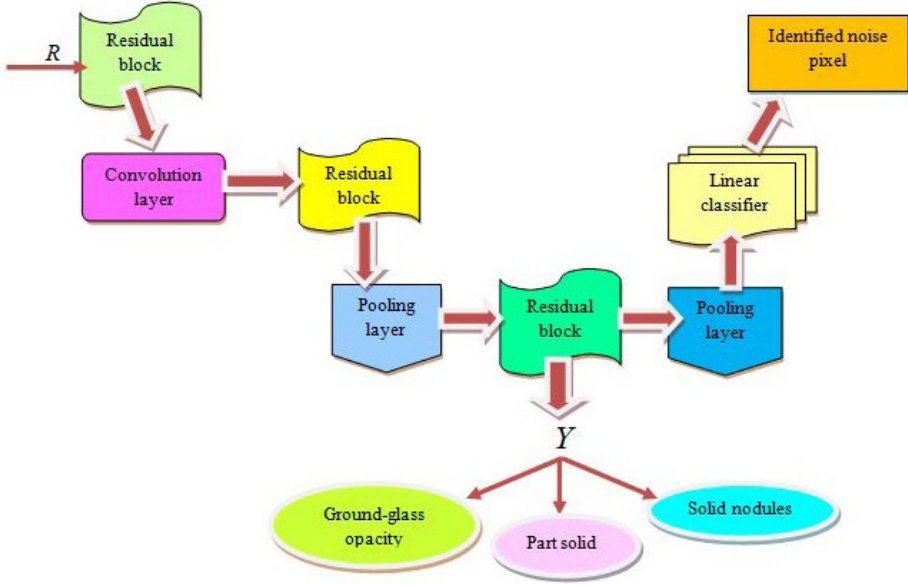
$$N = \Lambda N + \tau. \tag{32}$$

Fig. 2.   Structure of DRN.

Figure 2 reveals the DRN structure. It assists in discovering the lung nodule classes.

3.5.2. *DRN training using SSSCA*

The training process of DRN is carried out with the developed SSSCA. Here, SCA[22] is first developed with the mathematical model using sine and cosine functions. It is effective in making trade-offs among exploitation and exploration states to discover improved regions and assists in attaining a global optimal solution. The technique helps in avoiding the local optima and poses elevated exploration and thereby addresses the real-world problems. Meanwhile, SSOA[21] is motivated by the mimicking behavior of the shepherd. SSOA effectively balanced the exploitation and exploration capabilities. Furthermore, SSOA addressed the conventional engineering problems with enhanced accuracy. In addition, SSOA can determine the optimum solution with less assessment of some issues. Hence, the integration of SSOA and BA is done for enhancing the overall performance of the algorithm. The steps present in the technique are given as follows:

Step 1 (Initialization). The SSOA is fixed and the preliminary sheep position is discovered in a random manner in m-dimensional search space which is given as

$$U_x^0 = U_{\min} + \text{rand}(U_{\max} - U_{\min}) \quad \text{such that } x = 1, 2, \ldots, j. \tag{33}$$

Step 2 (Detection of error). The best solution is determined using the error. It is considered as a minimization problem for which the best solution is determined.

MSE is given by

$$\text{MS}_{\text{err}} = \frac{1}{k} \sum_{f=1}^{k} [\xi - Y]^2, \tag{34}$$

where $1 < f \leq k$.

Step 3 (Build herds). As per SSOA,[21] the sheep are divided into x herds each having y sheep. Thus $l = x \times y$. For splitting the sheep in each herd, the sorting of all sheep is done using the errors in ascending order for collecting them in the herd. The first y sheep are chosen and put arbitrarily in each herd.

Step 4 (Evaluate step size). The step size is evaluated by

$$\lambda_x = \mu \times \text{rand}(U_o U_x) + \eta \times \text{rand}(U_a - U_x), \tag{35}$$

where μ is formulated as

$$\mu = \mu_0 - \frac{\mu_0}{\text{Maxitn}} \times \text{itn}, \tag{36}$$

and η is formulated as

$$\eta = \eta_0 - \frac{\eta_{\max} - \eta_0}{\text{Maxitn}} \times \text{itn}. \tag{37}$$

Step 5 (Evaluate temple solution vector).

The SSOA is effective in addressing the global optimization problems. As per SSOA,[21] the temple solution vector is evaluated for each sheep and is given as

$$U_x^{\text{temple}} = U_x^{\text{old}} + \lambda_x. \tag{38}$$

The above equation can be rewritten by substituting the value of step size as

$$U(z+1) = U(z) + \mu \times \text{rand}(U_o - U(z)) + \eta \times \text{rand}(U_a - U(z)), \tag{39}$$

$$U(z+1) = U(z)[1 - \mu \times \text{rand} - \eta \times \text{rand}U_o + \eta \times \text{rand}U_a]. \tag{40}$$

The SCA is employed for solving real-world problems, as it averts local optima to explore the search space for optimum solution. According to SCA,[22] the solution update is modeled as

$$U(z+1) = U(z) + d_1 \sin(d_2) \times |d_3 Q - U(z)|. \tag{41}$$

Assume $QB > U(z)$, hence the equation is rewritten as

$$U(z+1) = U(z) + d_1 \sin(d_2) \times (d_3 QB - U(z)), \tag{42}$$

$$U(z) = \frac{U(z+1)d_1 \sin(d_2) \times d_3 QB}{1 - d_1 \sin(d_2)}. \tag{43}$$

Substituting Eq. (44) into Eq. (40),

$$U(z+1) = \frac{U(z+1)d_1 \sin(d-2) \times d_3 QB}{1 - d_1 \sin(d_2)}$$
$$\times [1 - \mu \times \text{rand} - \eta \times \text{rand}] + [\mu \times \text{rand}U_o + \eta \times \text{rand}U_a], \tag{44}$$

Table 2.   Pseudo-code of SSSCA.

Input: Population U
Output: Optimum solution U^*
Begin
Initialize the population U in a random manner
Compute error using Eq. (34)
Build herds
while stop criteria not satisfied do
For $(z < z_{\max})$
Evaluate step size using Eq. (35)
Evaluate temple solution vector using Eq. (38)
Update agent and merge solution using Eq. (46)
Update the control parameters using Eqs. (36) and (37)
End for
$z = z + 1$
Compute error using Eq. (34)
Return U^*

$$U(z+1) = \frac{1}{\mu \times \text{rand} + \eta \times \text{rand} d_1 \sin(d_2)}$$
$$\times (\mu \text{rand} U_o(1 - d_1 \sin(d_2)) + \eta \text{rand} U_a(1 - d_1 \sin(d_2)) - d_1 \sin(d_2)$$
$$\times d_3 QB \times [1 - \mu \text{rand} - \eta \text{rand}]). \tag{45}$$

The final proposed SSSCA equation is expressed as

$$U(z+1) = \frac{\begin{aligned}(1 - d_1 \sin(d_2))(\mu \text{rand} U_o + \eta \text{rand} U_a) + d_1 \sin(d_2)\\ \times d_3 QB[\mu \text{rand} + \eta \text{rand} - 1]\end{aligned}}{\mu \times \text{rand} + \eta \times \text{rand} d_1 \sin(d_2)}. \tag{46}$$

Step 6 (Re-evaluation of error).

The error is re-computed wherein weights linked with the least error are employed for training the DRN.

Step 7 (Terminate).

The optimal weights are generated frequently till the highest iteration is reached. Table 2 provides the pseudo-code of the proposed SSSCA.

The output obtained from the proposed SSSCA-based DRN is denoted by Y that helps to find the long nodule classes including GGO, part solid and solid nodules.

4. Results and Discussion

The effectiveness of SSSCA-based DRN is evaluated with specificity, sensitivity and testing accuracy by altering the training data and K-fold.

4.1. *Experimental setup*

The SSSCA-based DRN is processed on Windows 10 OS with 2-GB RAM and Intel Core processor and is functioned in Matlab.

4.2. *Dataset used*

The dataset used for the analysis is the Lung Image Database Consortium image collection (LIDC-IDRI) database.[18] It refers to the international resources utilized for the development, training process and computation of computer-aided design (CAD) techniques for the discovery and treatment of lung cancer. This database was developed by the National Cancer Institute (NCI). This database comprises 1 018 cases and is built by seven academic and eight medical imaging institutions.

4.3. *Experimental results*

Figure 3 reveals the experimental outcomes of the developed SSSCA-based DRN using a set of original images. The original input images are revealed in Fig. 3(a). The pre-processed image using ROI extraction and Wiener filter is displayed in Fig. 3(b). The segmented image is revealed in Fig. 3(c).
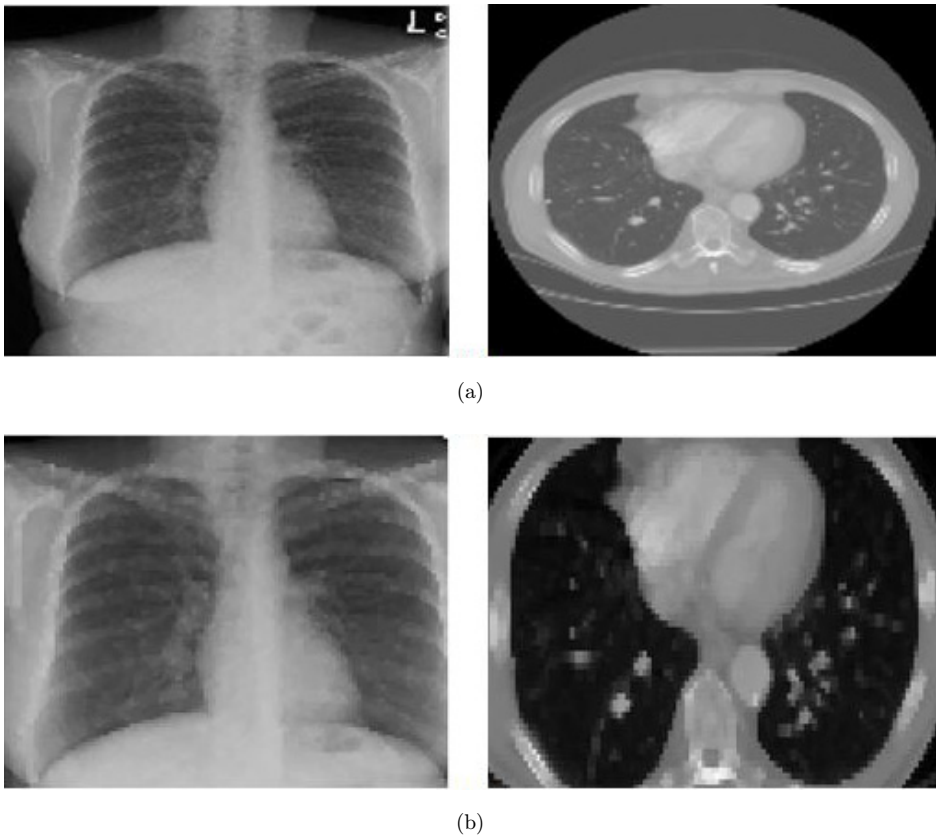

(a)

(b)

Fig. 3. Experimental results of the developed SSSCA-based DRN with (a) original input images, (b) pre-processed image using ROI extraction and Wiener filter and (c) segmented image.
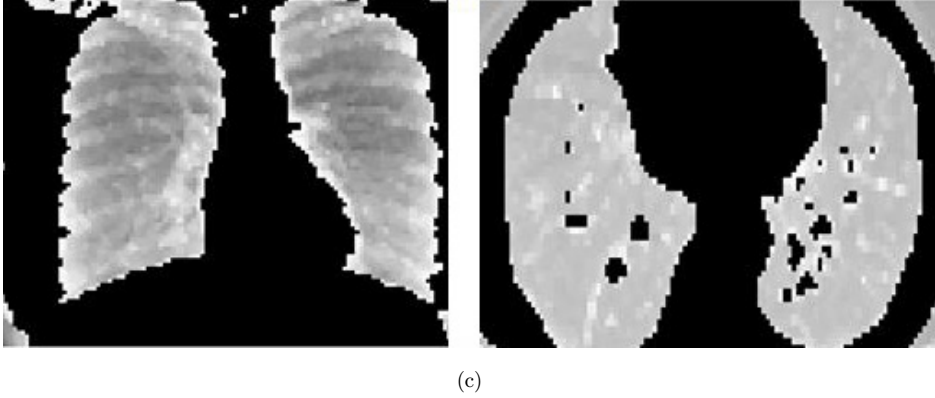
(c)

Fig. 3. (*Continued*)

4.4. *Evaluation measures*

The designed lung nodule classification model involves certain measures, which are illustrated below.

4.4.1. *Accuracy*

It symbolizes the closeness degree of the computed value to the original value in lung nodule classification, and is expressed as

$$\text{Accuracy} = \frac{c+d}{c+d+e+f}. \tag{47}$$

4.4.2. *Sensitivity*

It refers to the ratio of positives that are detected by the lung nodule classification technique and is formulated as

$$\text{Sensitivity} = \frac{c}{c+d}. \tag{48}$$

4.4.3. *Specificity*

It refers to the ratio of negatives determined using the designed model precisely, and is formulated as

$$\text{Specificity} = \frac{d}{d+f}. \tag{49}$$

4.4.4. F_1-*score*

It is defined as the harmonic mean of the devised approach's recall and precision, and is formulated by

$$F_1\text{-score} = \frac{c}{c+\frac{1}{2}(f+d)}. \tag{50}$$

4.5. *Performance assessment*

The inspection of the developed SSSCA-based DRN using specificity, sensitivity and testing accuracy by altering the training data and K-fold is explained below.

4.5.1. *Assessment with training data*

Figure 4 presents the assessment results of SSSCA-based DRN by altering the training data. The assessment of SSSCA-based DRN using testing accuracy is displayed in Fig. 4(a). For 60% data, the testing accuracies measured for SSSCA-based DRN with iterations 10, 20, 30 and 40 are 0.762, 0.796, 0.832 and 0.851. Also, for 90% data, the testing accuracies produced by SSSCA-based DRN with iterations 10, 20, 30 and 40 are 0.877, 0.909, 0.918 and 0.925. The assessment of SSSCA-based DRN using sensitivity is displayed in Fig. 4(b). For 60% data, the sensitivities produced by SSSCA-based DRN with iterations 10, 20, 30 and 40 are 0.786, 0.805, 0.834 and 0.863. Also, for 90% data, the sensitivities produced by SSSCA-based DRN with iterations 10, 20, 30 and 40 are 0.881, 0.897, 0.902 and 0.932. The assessment of SSSCA-based DRN using specificity is displayed in Fig. 4(c). For 60% data, the
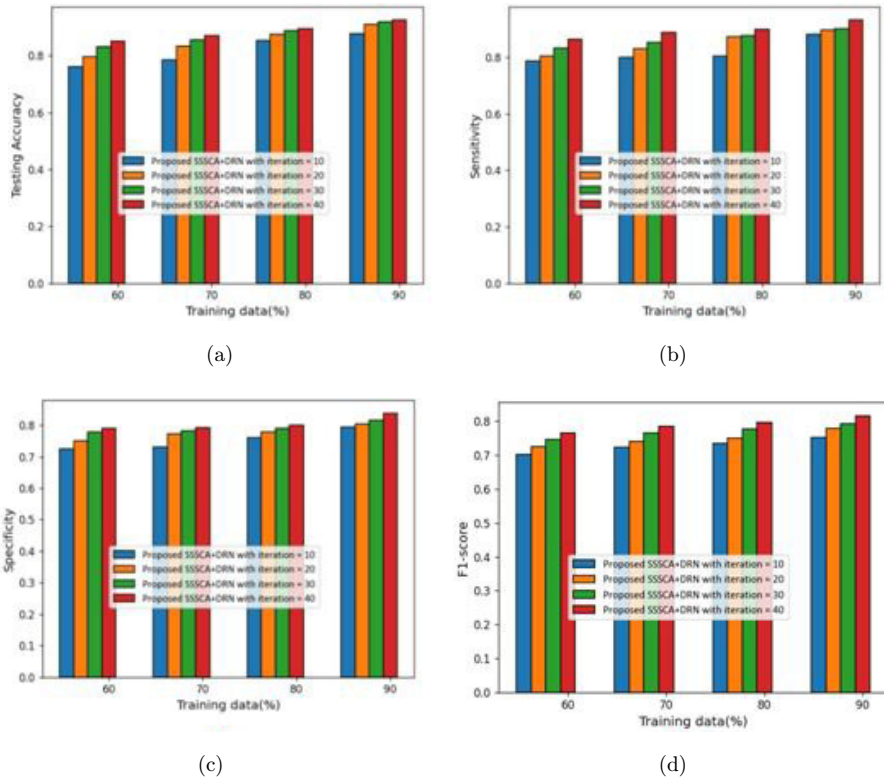

(a) (b) (c) (d)

Fig. 4. Assessment results of the developed SSSCA-based DRN by altering the training data using (a) testing accuracy, (b) sensitivity, (c) specificity and (d) F_1-score.

specificities produced by SSSCA-based DRN with iterations 10, 20, 30 and 40 are 0.725, 0.751, 0.779 and 0.791. Also, for 90% data, the specificities produced by SSSCA-based DRN with iterations 10, 20, 30 and 40 are 0.793, 0.804, 0.817 and 0.837. The performance analysis based on the F_1-score is provided in Fig. 4(d). The F_1-scores produced by SSSCA-based DRN with iterations 10, 20, 30 and 40 are 0.724, 0.740, 0.765 and 0.784, for 70% training data. Also, for 90% data, the F_1-score produced by SSSCA-based DRN with iterations 10, 20, 30 and 40 are 0.752, 0.778, 0.792 and 0.815. When considering the training percentage, the devised SSSCA-based DRN attained the highest results at 90% of training data.

4.5.2. *Assessment with K-fold*

The assessment results of the developed SSSCA-based DRN by altering the K-fold are revealed in Fig. 5. The assessment of the developed SSSCA-based DRN using testing accuracy is displayed in Fig. 5(a). For K-fold $= 5$, the testing accuracies produced by the developed SSSCA-based DRN with iterations 10, 20, 30 and 40 are 0.773, 0.791, 0.843 and 0.853. Also, for K-fold $= 8$, the testing accuracies produced by the developed SSSCA-based DRN with iterations 10, 20, 30 and 40 are 0.855,
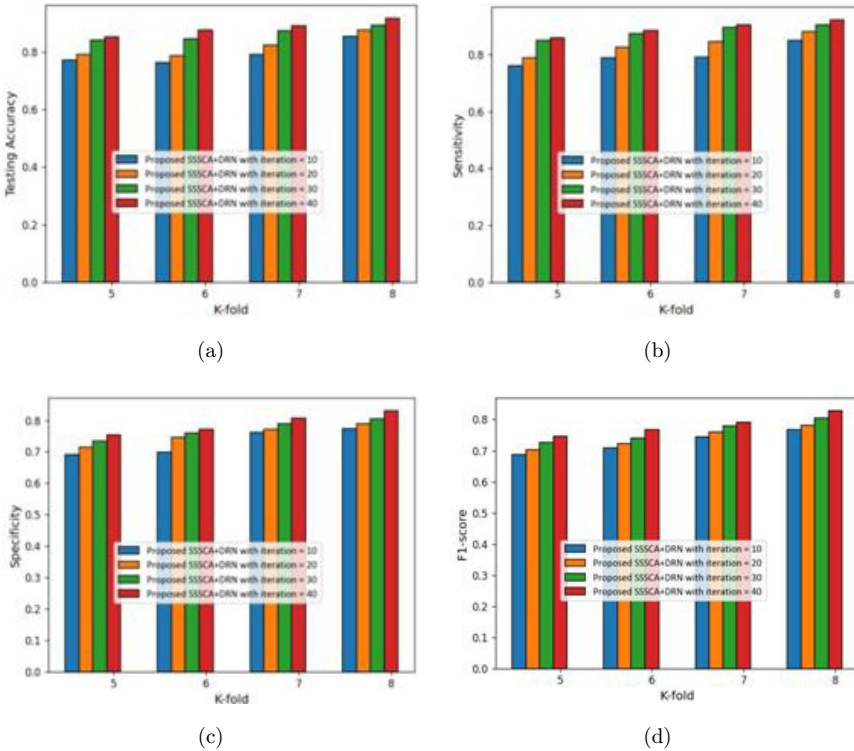

(a)

(b)

(c)

(d)

Fig. 5. Assessment results of the developed SSSCA-based DRN by altering the K-fold using (a) testing accuracy, (b) sensitivity, (c) specificity and (d) F_1-score.

0.876, 0.894 and 0.917. The assessment of the developed SSSCA-based DRN using sensitivity is displayed in Fig. 5(b). For K-fold = 5, the sensitivities produced by the developed SSSCA-based DRN with iterations 10, 20, 30 and 40 are 0.761, 0.790, 0.850 and 0.860. Also, for K-fold = 8, the sensitivities produced by the developed SSSCA-based DRN with iterations 10, 20, 30 and 40 are 0.851, 0.881, 0.905 and 0.922. The assessment of the developed SSSCA-based DRN using specificity is displayed in Fig. 5(c). For K-fold = 5, the specificities produced by the developed SSSCA-based DRN with iterations 10, 20, 30 and 40 are 0.690, 0.715, 0.735 and 0.753. Also, for K-fold = 8, the specificities produced by the developed SSSCA-based DRN with iterations 10, 20, 30 and 40 are 0.774, 0.789, 0.806 and 0.830. Figure 5(d) depicts the performance analysis based on the F_1-score. The F_1-scores produced by SSSCA-based DRN with iterations 10, 20, 30 and 40 are 0.709, 0.721, 0.740 and 0.767, for K-fold = 6. Also, for K-fold = 8, the F_1-scores produced by SSSCA-based DRN with iterations 10, 20, 30 and 40 are 0.768, 0.780, 0.805 and 0.827. When considering the K-fold, the devised SSSCA-based DRN attained the highest results at K-fold = 8.

4.6. *Comparative methods*

The comparison is done with the techniques including CNN,[3] DCT + CNN,[4] DTCNN,[6] ANN,[7] MSDLF[8] and the proposed SSSCA-based DRN.

4.7. *Comparative assessment*

The assessment results of techniques based on specificity, sensitivity, F_1-score and testing accuracy by varying the training data and K-fold are given in this subsection.

4.7.1. *Assessment with training data*

Figure 6 presents the assessment results by altering the training data. The assessment with testing accuracy is revealed in Fig. 6(a). For 60% data, the testing accuracies measured for CNN, DCT + CNN, DTCNN, ANN, MSDLF and SSSCA-based DRN are 0.699, 0.706, 0.772, 0.793, 0.827 and 0.851. Likewise, for 90% data, the testing accuracies produced by CNN, DCT + CNN, DTCNN, ANN, MSDLF and SSSCA-based DRN are 0.790, 0.814, 0.854, 0.879, 0.891 and 0.925. The performance improvements with respect to CNN, DCT + CNN, DTCNN, ANN and MSDLF of the developed SSSCA-based DRN using accuracy are 14.594%, 12%, 7.675%, 4.972% and 3.675%. The assessment using sensitivity is displayed in Fig. 6(b). For 60% data, the sensitivities produced by CNN, DCT + CNN, DTCNN, ANN, MSDLF and SSSCA-based DRN are 0.708, 0.723, 0.764, 0.785, 0.818 and 0.863. Also, for 90% data, the sensitivities produced by CNN, DCT + CNN, DTCNN, ANN, MSDLF and SSSCA-based DRN are 0.789, 0.833, 0.866, 0.889, 0.898 and 0.932. The performance improvements with respect to CNN, DCT + CNN, DTCNN, ANN and MSDLF of the developed SSSCA-based DRN using sensitivity are 15.343%, 10.622%, 7.081%,
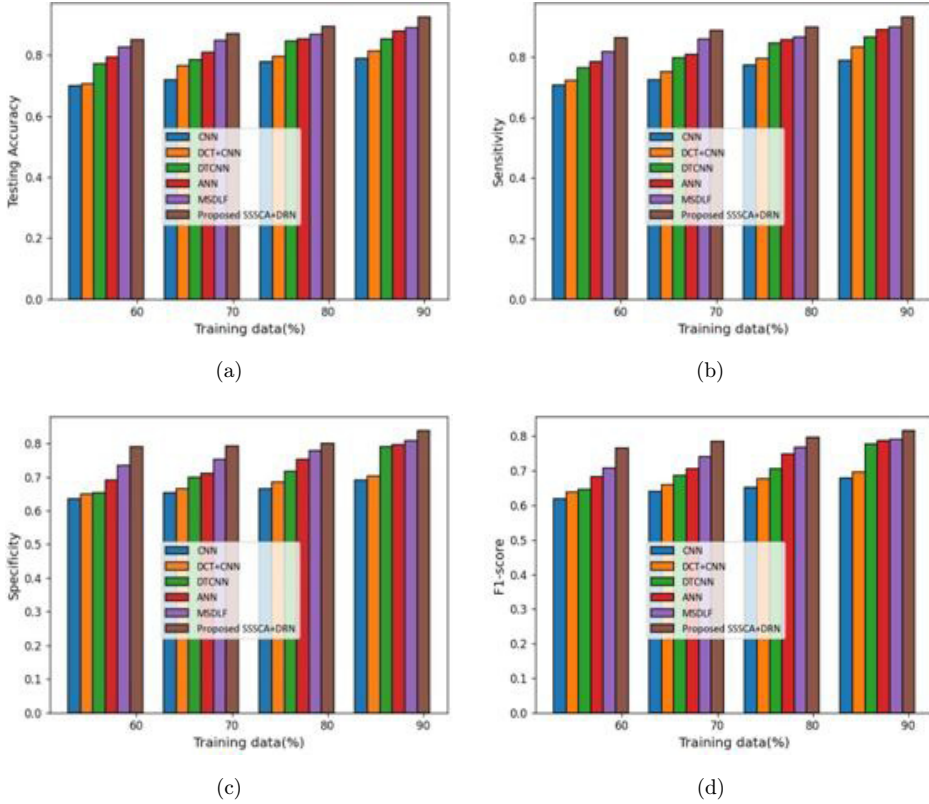
Fig. 6. Assessment results of different techniques by altering the training data using (a) testing accuracy, (b) sensitivity, (c) specificity and (d) F_1-score.

4.613% and 3.648%. The assessment using specificity is displayed in Fig. 6(c). For 60% data, the specificities produced by CNN, DCT + CNN, DTCNN, ANN, MSDLF and SSSCA-based DRN are 0.636, 0.650, 0.653, 0.692, 0.734 and 0.791. Also, for 90% data, the specificities evaluated for CNN, DCT + CNN, DTCNN, ANN, MSDLF and SSSCA-based DRN are 0.691, 0.703, 0.790, 0.796, 0.809 and 0.837. The performance improvements with respect to CNN, DCT + CNN, DTCNN, ANN and MSDLF of the developed SSSCA-based DRN using specificity are 17.443%, 16.009%, 5.615%, 4.898% and 3.345%. The F_1-score assessment is given in Fig. 6(d). For 70% data, the F_1-scores produced by CNN, DCT + CNN, DTCNN, ANN, MSDLF and SSSCA-based DRN are 0.640, 0.659, 0.687, 0.705, 0.741 and 0.784. Also, for 90% data, the F_1-scores evaluated for CNN, DCT + CNN, DTCNN, ANN, MSDLF and SSSCA-based DRN are 0.680, 0.696, 0.777, 0.786, 0.791 and 0.815. The performance improvements with respect to CNN, DCT + CNN, DTCNN, ANN and MSDLF of the developed SSSCA-based DRN using F_1-score are 16.64%, 14.64%, 4.72%, 3.61% and 2.93%.

4.7.2. *Assessment with K-fold*

Figure 7 presents the assessment results by altering the K-fold. The assessment using testing accuracy is displayed in Fig. 7(a). For K-fold $= 5$, the testing accuracies produced by CNN, DCT $+$ CNN, DTCNN, ANN, MSDLF and the developed SSSCA-based DRN are 0.692, 0.740, 0.772, 0.800, 0.832 and 0.853. Also, for K-fold $= 8$, the testing accuracies produced by CNN, DCT $+$ CNN, DTCNN, ANN, MSDLF and the developed SSSCA-based DRN are 0.782, 0.831, 0.855, 0.878, 0.891 and 0.917. The performance improvements with respect to CNN, DCT $+$ CNN, DTCNN, ANN and MSDLF of the developed SSSCA-based DRN using accuracy are 14.721%, 9.378%, 6.761%, 4.252% and 2.835%. The assessment with sensitivity is displayed in Fig. 7(b). For K-fold $= 5$, the sensitivities produced by CNN, DCT $+$ CNN, DTCNN, ANN, MSDLF and the developed SSSCA-based DRN are 0.693, 0.715, 0.756, 0.789, 0.832 and 0.860. Also, for K-fold $= 8$, the sensitivities produced by CNN, DCT $+$ CNN, DTCNN, ANN, MSDLF and the developed SSSCA-based DRN are 0.799, 0.830, 0.860, 0.896, 0.901 and 0.922. The performance
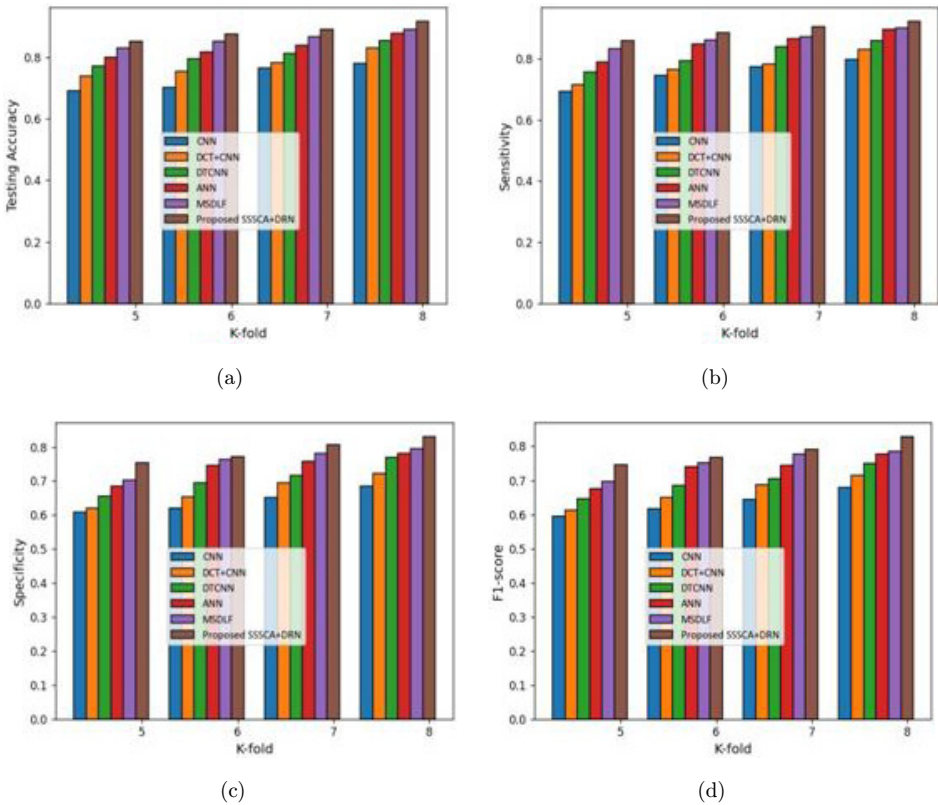

(a)　　　　　　　　　　　　　　　(b)

(c)　　　　　　　　　　　　　　　(d)

Fig. 7.　Assessment results of different techniques by altering the K-fold using (a) testing accuracy, (b) sensitivity, (c) specificity and (d) F_1-score.

improvements with respect to CNN, DCT + CNN, DTCNN, ANN and MSDLF of the developed SSSCA-based DRN using sensitivity are 13.340%, 9.978%, 6.724%, 2.819% and 2.277%. The assessment using specificity is displayed in Fig. 7(c). For K-fold = 5, the specificities produced by CNN, DCT + CNN, DTCNN, ANN, MSDLF and the developed SSSCA-based DRN are 0.608, 0.621, 0.655, 0.686, 0.704 and 0.753. Also, for K-fold = 8, the specificities produced by CNN, DCT + CNN, DTCNN, ANN, MSDLF and the developed SSSCA-based DRN are 0.685, 0.723, 0.770, 0.782, 0.796 and 0.830. The performance improvements with respect to CNN, DCT + CNN, DTCNN, ANN and MSDLF of the developed SSSCA-based DRN using specificity are 17.469%, 12.891%, 7.228%, 5.783% and 4.096%. The F_1-score assessment is depicted in Fig. 7(d). For K-fold = 6, the F_1-scores produced by CNN, DCT + CNN, DTCNN, ANN, MSDLF and SSSCA-based DRN are 0.616, 0.649, 0.684, 0.739, 0.752 and 0.767. Also, for K-fold = 8, the F_1-scores evaluated for CNN, DCT + CNN, DTCNN, ANN, MSDLF and SSSCA-based DRN are 0.679, 0.715, 0.750, 0.778, 0.785 and 0.827. The performance improvements with respect to CNN, DCT + CNN, DTCNN, ANN and MSDLF of the developed SSSCA-based DRN using F_1-score are 17.95%, 13.55%, 9.41%, 5.99% and 5.09%.

4.8. *Comparative discussion*

Table 3 reveals the assessment by varying the training data and K-fold. Using training data, an elevated testing accuracy of 0.925 is produced by the developed SSSCA-based DRN, whereas the accuracies produced by CNN, DCT + CNN, DTCNN, ANN and MSDLF are 0.790, 0.814, 0.854, 0.879 and 0.891. An elevated sensitivity of 0.932 is measured for the developed SSSCA-based DRN whereas the sensitivities measured for CNN, DCT+CNN, DTCNN, ANN and MSDLF are 0.789, 0.833, 0.866, 0.889 and 0.898. The highest specificity of 0.837 is measured for the developed SSSCA-based DRN, whereas the specificities measured for CNN, DCT + CNN, DTCNN, ANN and MSDLF are 0.691, 0.703, 0.790, 0.796 and 0.809. The maximum F_1-score of 0.815 is measured for the developed SSSCA-based DRN, whereas the F_1-scores measured for CNN, DCT + CNN, DTCNN, ANN and MSDLF are 0.680, 0.696, 0.777, 0.786 and 0.791. Using K-fold, the elevated testing accuracy

Table 3. Comparison of acoustics for frequencies for the piston–cylinder problem.

Data	Metric	CNN	DCT + CNN	DTCNN	ANN	MSDLF	Proposed SSSCA-based DRN
Training data	Testing accuracy	0.790	0.814	0.854	0.879	0.891	0.925
	Sensitivity	0.789	0.833	0.866	0.889	0.898	0.932
	Specificity	0.691	0.703	0.790	0.796	0.809	0.837
	F_1-score	0.680	0.696	0.777	0.786	0.79	0.815
K-fold	Testing accuracy	0.782	0.831	0.855	0.878	0.891	0.917
	Sensitivity	0.799	0.830	0.860	0.896	0.901	0.922
	F_1-score	0.680	0.696	0.777	0.786	0.791	0.815

of 0.917, sensitivity of 0.922, specificity of 0.830 and F_1-score of 0.827 are measured for the developed SSSCA-based DRN.

5. Conclusion

An optimization-driven deep model is devised to classify the nodules of the lung. Preprocessing is done by the extraction of ROI and adaptive Wiener filter to eliminate noise. Segmentation is performed with the DeepJoint model wherein the distance is computed using the congruence coefficient for mining the segments. The discovery of nodules is done with the grid-based scheme. Then, the mining of essential features is performed for improved processing. Here, the features like GBP features, Texton features, short axis and long axis, barycenter difference, perimeter and area, number of slices, volume and statistical features are considered. The lung nodule classification is done with DRN. The DRN training is performed with the proposed SSSCA. The proposed SSSCA is developed by integrating SCA and SSOA. Here, the proposed SSSCA-based DRN is used to classify the lung nodules as part solid, solid nodules and GGO. The proposed SSSCA-based DRN outperformed with the highest testing accuracy of 92.5%, sensitivity of 93.2%, specificity of 83.7% and F_1-score of 81.5%. In the future, other databases can be utilized for checking the feasibility of the proposed model.

References

1. C. N. Aher and A. K. Jena, Soft computing based approaches for classifying diseases using medical diagnosis dataset, in *Proc. Int. Conf. Emerging Smart Computing and Informatics (ESCI)* (2020), pp. 77–81.
2. C. N. Aher and A. K. Jena, Rider-chicken optimization dependent recurrent neural network for cancer detection and classification using gene expression data, *Comput. Methods Biomech. Biomed. Eng., Imaging Vis.* **9**(2) (2021) 174–191.
3. F. M. AlBalushi, Bat optimization assisted diabetic retinopathy detection framework, *Multimed. Res.* **3**(2) (2020) 20–26.
4. M. Caricato, G. L. Baiocchi, F. Crafa, S. Scabini, G. Brisinda, M. Clementi, G. Sica, P. Delrio, G. Longo, G. Anania, N. de Manzini, P. Amodio, A. Lucchi, G. Baldazzi, G. Garulli, A. Patriti, F. Pirozzi, M. Pavanello, A. Carrara, R. Campagnacci, A. Liverani, A. Muratore, W. Siquini, R. De Luca, S. Mancini, F. Borghi, M. Di Cosmo, R. Persiani, C. Pedrazzani, M. Scaramuzzi, M. Scatizzi, N. Vettoretto, M. Totis, A. Gennai, P. Marini, M. Basti, M. Viola, G. Ruffo and M. Catarci, Colorectal surgery in Italy during the Covid19 outbreak: a survey from the iCral study group, *Updates Surg.* **72**(2) (2020) 249–257.
5. Z. Chen, Y. Chen, L. Wu, S. Cheng and P. Lin, Deep residual network based fault detection and diagnosis of photovoltaic arrays using current-voltage curves and ambient conditions, *Energy Convers. Manag.* **198** (2019) 111793.
6. R. V. M. da Nobrega, P. P. Reboucas Filho, M. B. Rodrigues, S. P. da Silva, C. M. J. M. D. Juúnior and V. H. C. de Albuquerque, Lung nodule malignancy classification in chest computed tomography images using transfer learning and convolutional neural networks, *Neural Comput. Appl.* **32**(15) (2020) 11065–11082.

7. G. L. F. da Silva, T. L. A. Valente, A. C. Silva, A. C. de Paiva and M. Gattass, Convolutional neural network-based PSO for lung nodule false positive reduction on CT images, *Comput. Methods Prog. Biomed.* **162** (2018) 109–118.

8. A. El Hassani, B. A. Skourt and A. Majda, Efficient lung nodule classification method using convolutional neural network and discrete cosine transform, *Int. J. Adv. Comput. Sci. Appl.* **12** (2021) 766–772.

9. I. Goodfellow, J. Pouget-Abadie, M. Mirza, B. Xu, D. Warde-Farley, S. Ozair, A. Courville and Y. Bengio, Generative adversarial nets, in *Advances in Neural Information Processing Systems*, Vol. 27 (Curran Associates, 2014), pp. 1–9.

10. K. He, X. Zhang, S. Ren and J. Sun, Deep residual learning for image recognition, in *Proc. 2016 IEEE Conf. Computer Vision and Pattern Recognition* (IEEE, 2016), pp. 770–778.

11. X. Huang, Q. Lei, T. Xie, Y. Zhang, Z. Hu and Q. Zhou, Deep transfer convolutional neural network and extreme learning machine for lung nodule diagnosis on CT images, *Knowl.-Based Syst.* **204** (2020) 106230.

12. A. Kaveh and A. Zaerreza, Shuffled shepherd optimization method: a new meta-heuristic algorithm, *Eng. Comput.* **37** (2020) 2357–2389.

13. C. F. J. Kuo, C. C. Huang, J. J. Siao, C. W. Hsieh, V. Q. Huy, K. H. Ko and H. H. Hsu, Automatic lung nodule detection system using image processing techniques in computed tomography, *Biomed. Signal. Process.* **56** (2022) 101659.

14. G. H. Liu and J. Y. Yang, Image retrieval based on the texton co-occurrence matrix, *Pattern Recognit.* **41**(12) (2008) 3521–3527.

15. S. Mirjalili, SCA: a sine cosine algorithm for solving optimization problems, *Knowl.-Based Syst.* **96** (2016) 120–133.

16. P. Monkam, S. Qi, M. Xu, F. Han, X. Zhao and W. Qian, CNN models discriminating between pulmonary micro-nodules and non-nodules from CT images, *Biomed. Eng. Online* **17**(1) (2018) 96.

17. K. S. Praveena, A classical hierarchy method for bone X-ray image classification using SVM, *Int. Res. J. Eng. Technol.* **04** (2017) 991–993.

18. B. Pu, K. Li, S. Li and N. Zhu, Automatic fetal ultrasound standard plane recognition based on deep learning and IIoT, *IEEE Trans. Ind. Inform.* **17**(11) (2021) 7771–7780.

19. B. Pu, N. Zhu, K. Li and S. Li, Fetal cardiac cycle detection in multi-resource echocardiograms using hybrid classification framework, *Future Gener. Comput. Syst.* **115**(3) (2021) 825–836.

20. M. I. Razzak, S. Naz and A. Zaib, Deep learning for medical image processing: Overview, challenges and the future, in *Classification in BioApps*, Lecture Notes in Computational Vision and Biomechanics, Vol. 26 (Springer, 2018), pp. 323–350.

21. A. Renjit, DeepJoint segmentation for the classification of severity-levels of glioma tumour using multimodal MRI images, *IET Image Process.* **14**(11) (2020) 2541–2552.

22. A. Sarkar, Optimization assisted convolutional neural network for facial emotion recognition, *Multimed. Res.* **3**(2) (2020) 35–41.

23. T. Sathiya and B. Sathiyabhama, Fuzzy relevance vector machine based classification of lung nodules in computed tomography images, *Int. J. Imaging Syst. Technol.* **29**(3) (2019) 360–373.

24. Scholarpedia.org, Deep belief networks (2009), http://scholarpedia.org/article/Deep_belief_networks.

25. A. Taghipour, B. Glaa and N. Zoghlami, Network coordination with minimum risk of information sharing, in *Proc. Int. Conf. Advanced Logistics and Transport (ICALT)* (2014).

26. The Lung Image Database Consortium, Cancer Imaging Archive (LIDC-IDRI) (2021), https://wiki.cancerimagingarchive.net/display/Public/LIDC-IDRI.

27. M. Z. ur Rehman, M. Javaid, S. I. A. Shah, S. O. Gilani, M. Jamil and S. I. Butt, An appraisal of nodules detection techniques for lung cancer in CT images, *Biomed. Signal Process. Control* **41** (2018) 140–151.

28. B. K. Veronica, An effective neural network model for lung nodule detection in CT images with optimal fuzzy model, *Multimed. Tools Appl.* **79** (2020) 14291–14311.

29. W. Wang, G. Chen, H. Chen, T. T. A. Dinh, J. Gao, B. C. Ooi, K. L. Tan, S. Wang and M. Zhang, Deep learning at scale and at ease, *ACM Trans. Multimed. Comput. Commun. Appl.* **12** (2016) 69.

30. Q. Wang, F. Shen, L. Shen, J. Huang and W. Sheng, Lung nodule detection in CT images using a raw patch-based convolutional neural network, *J. Digit. Imaging* **32**(6) (2019) 971–979.

31. P. Wu, X. Sun, Z. Zhao, H. Wang, S. Pan and B. Schuller, Classification of lung nodules based on deep residual networks and migration learning, *Comput. Intell. Neurosci.* **2020** (2020) 8975078.

32. G. Xiao, J. Li, Y. Chen and K. Li, MalFCS: An effective malware classification framework with automated feature extraction based on deep convolutional neural networks, *J. Parallel Distrib. Comput.* **141** (2020) 49–58.

33. Q. Zhang and X. Kong, Design of automatic lung nodule detection system based on multi-scene deep learning framework, *IEEE Access* **8** (2020) 90380–90389.

P. Chinniah was born in India in 1966. He received his B.Tech. degree in Electronics Engineering and M.E. degree in Medical Electronics from Anna University, Chennai, Tamil Nadu, India in 1992 and 1998, respectively. He received his Ph.D. degree on "A Study and Application of Medical Standards in a Collaborative Healthcare Information System" from Anna University, Chennai. He is currently working as a Professor in the Department of Electronics & Communication Engineering, St. Joseph College of Engineering, Chennai, Tamil Nadu, India. He has 22 years of teaching experience. His research interests are in medical informatics, medical standards, e-health and medical expert systems.

Balajee Maram earned his Master's degree in Computer Science and Engineering from Anna University, Chennai, Master of Business Administration degree from Alagappa University, Karaikudi, M.A. (Master of Communication and Journalism) degree from Alagappa University, Karaikudi and doctoral degree from Bharathiar University, Coimbatore. He is currently working as an Associate Professor in the Department of Computer Science and Engineering, Chitkara University School of Engineering and Technology, Chitkara University, Baddi, Himachal Pradesh, India. He has more than 15 years of teaching experience, five years of industry experience and six years of research experience. He has published 50 research papers

in reputed journals which are indexed by both SCIE and SCOPUS. He has guided 14 UG projects and twoPG projects. He has filed for four-Indian patents and been granted two Australian patents. He has organized one national workshop and one national conference. He has published five book chapters indexed by SCOPUS. He has authored three books titled "Data Communication and Networking" and "XML & Web-Services". He has received the "Best Researcher Award 2018" from DK International Research Foundation, the "Best Researcher Award 2018" in the 117th International Research Awards on Engineering, Science and Management and "Outstanding Researcher" award from the International Institute of Organized Research (I2OR), India and Australia, in December 2018. He has the professional memberships of CSI, ISTE, CRSI, IACSIT, UACEE and CSTA. His research interests are in cryptography, cloud computing, big data analytics and security in IoT. He has submitted the research project proposals to DST and SERB agencies in 2018–2021.

P. Velrajkumar obtained his B.E. degree in Electrical and Electronics Engineering in 1997 from Noorul Islam College of Engineering, India. He obtained his M.E. degree in Applied Electronics in 1999 from Hindustan College of Engineering, India. He has over 22 years of teaching experience and around a decade of research experience. He also possesses 16 years of international experience in teaching and research. Currently, he is working as an Associate Professor and Head of the Centre of Excellence:Intelligent Robotic Systems in the Department of Electrical and Electronics Engineering, CMR Institute Technology, Bengaluru, Karnataka, India. His areas of interests include control systems, robotics and automation. He served as a reviewer in international journals and a committee member in various international conferences. His professional memberships are: Senior Member, IEEE and Member, IET (UK).

Ch. Vidyadhari currently working as an Assistant Professor in the Department of Information Technology, Gokaraju Rangaraju Institute of Engineering and Technology, Bachupally, Kukatpally, Hyderabad, Telangana, India. She obtained her M.Tech. degree (Software Engineering) from Aurora's Engineering College, Hyderabad in the year 2008. She has completed her Ph.D. in Computer Science and Engineering from JNTU College of Engineering, Kakinada. Her areas of research interest include text mining, machine learning, data science and natural language processing. She has published around 10 papers in reputed international journals and has an experience of 15 years in teaching. She has been certified as an Oracle-Certified Java Standard Edition 6 Programmer (OCJP) and an Oracle-Certified Associate (OCA). She received the best researcher award from Gokaraju Rangaraju Institute of Engineering and Technology.